Mechanical Systems and Signal Processing 140 (2020) 106655

Contents lists available at ScienceDirect

Mechanical Systems and Signal Processing

journal homepage: www.elsevier.com/locate/ymssp

Identifying the presence of structural damage: A statistical hypothesis testing approach combined with residual strain energy

Shuqing Wang [a], Haoyu Wang [a], Mingqiang Xu [a,*], Jian Guo [a]

[a] Shandong Provincial Key Laboratory of Ocean Engineering, Ocean University of China, 266100, China

ARTICLE INFO

Article history:
Received 25 July 2019
Received in revised form 31 October 2019
Accepted 13 January 2020

Keywords:
Damage detection
Environmental variation
Statistical hypothesis testing
Residual strain energy
Sensitivity analysis
Degree of freedom

ABSTRACT

A statistical hypothesis testing scheme is presented for damage detection considering environmental variations, in which the presence of damage is identified via Welch's t-test by comparing the means of two groups of residual strain energy (RSE) samples from healthy and inspected structures. The RSE, as a damage indication feature, is determined from the mode shape residual (MSR), and the corresponding effects of environmental variations are eliminated via the PCA method. To further improve the damage sensitivity of RSE samples, an MSR selection strategy is proposed to examine the sensitivity of the available MSR matrices to damage and select the most effective MSR matrix. The sensitivity formula of the test statistic with respect to damage is derived and defined as the sensitivity index. Moreover, the mode shape expansion process is not required because an MSR that only includes *x*- or *y*-translational degrees of freedom (DoFs) at the measured points is sufficient for detecting damage. The effects of the location and extent of damage, incomplete measurements, and the critical value of the t-test on the performance of the proposed scheme are discussed by numerically analyzing an offshore platform. The results indicate that the scheme can simultaneously limit the probability of committing Type I and Type II errors under temperature variations and noise contamination. An analysis of field test data for a real-world wind turbine also indicates that this approach can avoid Type I error in a real marine environment.

1. Introduction

The complexity and size of large-scale ocean engineering structures, such as offshore jacket platforms and offshore turbines, as well as their harsh working environment make structural health monitoring (SHM) indispensable to ensure structural safety and durability [1–5]. Vibration-based damage identification as a field of SHM has been widely investigated in past decades, and the basic concept is that the modal parameters (notably natural frequencies, mode shapes, and modal damping) change due to the alteration of the physical properties of a structure [6,34]. Such changes identified from the modal parameters can be used to reflect the real state of the structure. Among the available mode shape-based damage identification methods, modal strain energy (MSE) methods seem promising due to their high sensitivity to structural damage. Stubbs et al. [8] proposed an MSE-based damage index for the field-tested nondestructive damage evaluation of the I-40

* Corresponding author.
E-mail address: xumingqiang@stu.ouc.edu.cn (M. Xu).

https://doi.org/10.1016/j.ymssp.2020.106655
0888-3270/

Bridge. The damage locations predicted by the index display a strong correlation with the visually observed surface crack pattern [9]. Shi et al. [10,11] proposed a modal strain energy change ratio (MSECR) method, and the sensitivity to the damage location was theoretically proven and verified by a laboratory 2-D structure. The MSECR method is a very simple but efficient tool for damage localization and has thus been widely adopted in two-stage damage identification methods. Yan and Ren [12] derived the first-order sensitivity formulae of the MSE of elements for a real symmetric undamped structural system. Based on the closed form of element MSE sensitivity, a statistical structural damage detection algorithm was proposed [13]. The method was oriented to the ambient vibration measurements, and only the operational mode shapes were available. To overcome the limitations associated with localizing and identifying the extent of multiple damage areas with low accuracy and abundant noise, Cha and Buyukozturk [14] modified the form of MSE by using the absolute value of mode shapes. They proposed a GA-based hybrid multiobjective optimization approach for damage detection [15], and the change in the modified MSE between the damage-induced structure and the damage-simulated structure was expressed by the objective functions of the NS2-IRR GA. Dessi and Camerlengo [16] and Wang and Xu [17] reviewed the available MSE-based damage detection methods and summarized guidelines for using these methods. (see [7]).

Damage identification is a problem that can be addressed at many levels. Stated in its most basic form, the objective is to identify if damage is present or not. One class of algorithms that shows considerable promise for this purpose is novelty detection techniques. The philosophy is simple; during the normal operation of a structure, features are extracted from measurement data, which are used to characterize the healthy condition. When the structure needs to be inspected, data from the structure can be examined to determine whether the current features deviate significantly from the healthy. An alarm is signaled if the defined index value increases above a predetermined threshold [18]. This study aims to identify the presence of damage with a novelty detection technique in which an index is defined by an MSE-like quantity.

In practical situations, civil and ocean engineering structures are subject to varying environmental conditions that mask the changes in the structural dynamic features caused by damage and result in false positive or false negative damage detection. The related research regarding the effects of these conditions on bridge structures is extensive. Wood [19] reported that the changes in bridge responses were closely related to the structural temperature based on field test data, which suggested that the variability in the asphalt elasticity modulus due to temperature effects is a major contributor to the changes in the structural stiffness. Peeters and De Roeck [20] performed one-year monitoring on the Z24 Bridge and found that the influence of temperature variation became prominent when the temperature fell below the freezing point. Xia et al. [21] conducted an experimental study of an RC slab to investigate the variations in modal properties with respect to temperature and humidity changes. It was found that the frequencies have a strong negative correlation with temperature and humidity and damping ratios have a positive correlation with these factors, but no clear correlation between mode shapes and temperature or humidity changes was observed. Wind is also a key factor that influences the dynamic features of large-scale structures because the energy input from wind-induced vibration sometimes becomes larger than the energy dissipated by damping, causing flutter or buffeting. Mahmoud et al. [22] found that the vertical amplitude of a bridge response is almost a quadratic function of the wind speed. Local scouring around the structural foundation caused by a flood commonly leads to changes in boundary conditions and influences the dynamic features of the structure [23]. The effects of various changing environmental and operational conditions are more severe for offshore platform structures in harsh marine environments, and specialized research is rarely reported. In addition to the factors mentioned above, tidal actions mainly result in added mass changes based on the relevant fluid-structure interaction function, which indirectly changes the mass of an offshore platform to some degree. In addition, marine growth directly and indirectly increases the mass of offshore platforms and damping behavior due to changes in the structural surface roughness.

The issue of damage detection under varying environmental conditions has attracted increasing attention, and to date, two methods have been proposed to address this issue. One of the methods is to perform a correlation analysis between the measured vibration features and the potential changes in environmental conditions. In the development of these methods, the healthy state of the structure is parameterized to reflect the different environmental and operational conditions, and the structural damages are only responsible for the additional changes in these features. Peeters et al. [24] used the prediction error of the ARX model as an indicator of damage features to determine the real state of the structure. Moser and Moaveni [25] proposed several nonlinear models to represent the relationship between the identified natural frequencies and measured temperatures. Bao et al. [26] revealed the relation between the natural frequencies and temperature with an experimental framework, and a linear regression model between the frequency and temperature was established to eliminate temperature effects. Nevertheless, these methods are subject to several practical drawbacks. As noted by Kullaa [27], the optimal locations of temperature sensors are often difficult to determine and reach, although temperature measurements are relatively easy to record. In addition, to establish the correlation between the measured features and the environmental variables, the sensors that measure the environmental variables must remain in the same configuration. Any of these failures may cause problems in the detection of the presence of damage. These methods are thus not always applicable to large-scale engineering structures subject to heterogeneous environmental conditions at various points on the structure.

Compared with the first set of methods, the second set analyzes only the identified modal features regardless of the measured environmental conditions, and these methods show promise. The typical algorithms include cointegration analysis (CA), factor analysis (FA), independent component analysis (ICA) and PCA. Recently, CA has been successfully implemented in the context of SHM, where it has been used to remove the confounding influences of environmental and operational variations [28]. To improve the power in modeling systems where measurands are nonlinearly related, Shi et al. [29] extended the well-established cointegration method to a nonlinear context to create a breakpoint in the cointegrating vector. A

simulated case and real SHM data from the Z24 Bridge both illustrated that environmental and operational variations can be efficiently eliminated by the proposed cointegration method. Deraemaeker et al. [30] used FA to remove the influence of temperature factors on natural frequencies and mode shapes and then used statistical process control with the multivariate Shewhart-T control charts to detect damage. PCA, as a data feature extraction and dimension reduction method, is widely used in the field of structural damage detection. Yan et al. [31] applied the PCA algorithm to a simulated concrete bridge subjected to temperature variations. They used natural frequencies as the raw data for damage detection and successfully identified the structural damage effect based on the residual error. Mujica et al. [32] proposed a comprehensive statistical analysis for SHM with random measurement errors; in this method, PCA was used for the sensor data from the undamaged structure to establish a baseline model space. When the structure needs to be inspected, new experiments, as a series of random processes, are performed, and the sensor data are projected into the baseline PCA model. Damage is then detected by analyzing whether the distribution of samples from the random processes associated with the current structure is related to that for the undamaged structure, i.e., a process of hypothesis testing. Recently, Mujica et al. [33] proposed a damage detection strategy based on ultrasonic guided waves for structures subjected to uniform temperature changes; in this method, a robust PCA orthogonal distance is selected as a damage feature. Xu et al. [34] used the PCA algorithm to eliminate the influence of environmental variations and further employed MSRs to construct a damage indicator for damage localization.

This study focuses on the development of a statistical hypothesis testing scheme for damage detection. The effects of temperature variations and noise contamination are both considered. Unlike many other methods, the mode shape rather than the natural frequency of the structure is used as the raw data for damage detection because the mode shape is confirmed to be more sensitive to damage [35] but robust to environmental variations, such as temperature changes [26]. As stated before, the use of hypothesis testing is not new in this field. The novelties of this paper are summarized as follows. (1) The RSE of the structure, constructed by the MSR, is selected as a damage-sensitive feature and defined as a random sample for the hypothesis testing scheme. (2) The sensitivity formula of the test statistic with respect to damage is derived and defined as the sensitivity index, and it is used to select the most effective MSR to construct the RSE samples. (3) Only the *x*- and *y*-translational DoFs at the measured points are required to construct the MSE, thereby reducing the difficulty of data collection and avoiding mode shape expansion errors.

In the following sections, the theoretical background of the statistical hypothesis testing scheme is described. Then, the hypothesis testing method incorporating the MSR selection strategy is introduced in detail. A numerical study and a real-world application are used to validate the proposed statistical hypothesis testing scheme. Finally, conclusions are drawn, and remarks are made on future work.

2. Theoretical backgrounds

2.1. PCA algorithm

PCA is a data dimension reduction and feature extraction algorithm, which can transform the original sample data into a set of linearly uncorrelated load vectors through linear transform. In the present work, it is used to extract the influence of environmental variations on mode shapes.

One denotes the j-th mode shape of q-th $(q = 1, 2, \cdots, N_q)$ measurement by vector $\phi_{j,q} \in \mathbb{R}^{N_n \times 1}$, where N_q and N_n are the numbers of vibration measurements and measured DoFs, respectively. The mode shapes obtained from each measurement are arranged into a matrix $\mathbf{\Phi}_j = \left[\phi_{j,1}, \phi_{j,2}, \cdots, \phi_{j,q}, \cdots, \phi_{j,N_q}\right], \mathbf{\Phi}_j \in \mathbb{R}^{N_n \times N_q}$; then, $\mathbf{\Phi}_j$ is centered to obtain a new matrix $\mathbf{\Upsilon}_j \in \mathbb{R}^{N_n \times N_q}$, for which the mean value of each row is equal to zero [34]. Here, the matrix $\mathbf{\Upsilon}_j \mathbf{\Upsilon}_j^T$ is proportional to the covariance matrix of matrix $\mathbf{\Upsilon}_j$. Eigenvalue decomposition is performed for $\mathbf{\Upsilon}_j \mathbf{\Upsilon}_j^T$:

$$\mathbf{\Gamma U} = \mathbf{\Upsilon}_j \mathbf{\Upsilon}_j^T \mathbf{U} \tag{1}$$

where $\mathbf{U}$ is an N_n-by-N_n matrix, whose columns are orthogonal unit vectors, called the eigenvectors of matrix $\mathbf{\Upsilon}_j \mathbf{\Upsilon}_j^T$.

$$\mathbf{U} = \{\boldsymbol{u}_1, \boldsymbol{u}_2, \ldots, \boldsymbol{u}_k, \ldots, \boldsymbol{u}_{N_n}\} \tag{2}$$

The eigenvectors define the principal components, each of which represents a main direction of variation due to an independent factor that influences the original data, i.e., an environmental condition. The diagonal matrix $\mathbf{\Gamma} \in \mathbb{R}^{N_n \times N_n}$ is the eigenvalue matrix of $\mathbf{\Upsilon}_j \mathbf{\Upsilon}_j^T$, and the diagonal element represents the energy of the corresponding principal components. The eigenvalues can be arranged in descending order.

$$\gamma_1 \geqslant \gamma_2 \geqslant \cdots \geqslant \gamma_k \geqslant \gamma_{k+1} \geqslant \cdots \geqslant \gamma_{N_n} \tag{3}$$

Assuming $\gamma_k \gg \gamma_{k+1} \to 0$, the first k principal components summarize most of the variance in the vibration features are necessary to consider. Conversely, the remainder (e.g., noise) of the components, with negligible influence, can be eliminated. The order k is closely related to the number of environmental variables; however, the guideline to selecting a proper k value is not discussed herein because the number of environmental variables is known in this study. The first k columns of $\mathbf{U}$ can be used to build a matrix $\mathbf{U}'$ that can be written as follows:

$$\mathbf{U}' = \{\boldsymbol{u}_1, \boldsymbol{u}_2, \ldots, \boldsymbol{u}_k\} \tag{4}$$

where $\mathbf{U}' \in \mathbb{R}^{N_n \times k}$ is called the loading matrix. The PCA method provides a linear mapping of the data from the original N_n-dimension space to a lower k-dimension space. A linear projection given by Eq. (4) maps the measured features $\boldsymbol{\Upsilon}_j^T$ into the space of environmental variable:

$$\mathbf{Z} = \boldsymbol{\Upsilon}_j^T \mathbf{U}' \tag{5}$$

where $\mathbf{Z} \in \mathbb{R}^{N_q \times k}$ is called the scored matrix. Then, the loss of information in this projection can be assessed by remapping the projected data back to the original space:

$$\widehat{\boldsymbol{\Upsilon}}_j = \left[\mathbf{Z}\left(\mathbf{U}'\right)^T\right]^T = \left[\boldsymbol{\Upsilon}_j^T \mathbf{U}' \left(\mathbf{U}'\right)^T\right]^T, \quad \widehat{\boldsymbol{\Upsilon}} \in \mathbb{R}^{N_n \times N_q} \tag{6}$$

2.2. Definition of RSE

According to the principle of the PCA algorithm introduced in Section 2.1, if $\boldsymbol{\Upsilon}_j$ represents the measured vibration feature of a healthy offshore platform as designated in Section 4.1, then $\widehat{\boldsymbol{\Upsilon}}_j$ is the change in the vibration feature caused by environmental variations. An MSR matrix $\boldsymbol{\Phi}_j$, which can more accurately reflect the healthy state of the healthy structure compared with the originally identified mode shape matrix $\boldsymbol{\Upsilon}_j$, can be defined as follows:

$$\boldsymbol{\Psi}_j = \boldsymbol{\Upsilon}_j - \widehat{\boldsymbol{\Upsilon}}_j, \quad \boldsymbol{\Psi}_j \in \mathbb{R}^{N_n \times N_q} \tag{7}$$

with column vectors that correspond to the measured mode shape vectors of the healthy structure.

$$\boldsymbol{\Psi}_j = \left[\psi_{j,1}, \psi_{j,2}, \cdots \psi_{j,q}, \cdots \psi_{j,N_q}\right] \tag{8}$$

When the offshore platform structure need to be inspected (healthy or not), likewise, the MSR matrix of j-th mode can be defined and arranged as follows:

$$\boldsymbol{\Psi}_j^* = \left[\psi_{j,1}^*, \psi_{j,2}^*, \cdots \psi_{j,q}^*, \cdots, \psi_{j,N_q}^*\right] \tag{9}$$

where the superscript "$*$" indicates a version of the inspected structure.

The general MSEs of the healthy and inspected structures are defined as

$$M_{j,q} = \left(\phi_{j,q}\right)^T \mathbf{K} \phi_{j,q}; \quad M_{j,q}^* = \left(\phi_{j,q}^*\right)^T \mathbf{K} \phi_{j,q}^* \tag{10}$$

where $\mathbf{K}$ is the overall stiffness matrix of the healthy structure. Likewise, the RSEs can be defined as

$$R_{j,q} = \left(\psi_{j,q}\right)^T \mathbf{K} \psi_{j,q}; \quad R_{j,q}^* = \left(\psi_{j,q}^*\right)^T \mathbf{K} \psi_{j,q}^* \tag{11}$$

where $R_{j,q}$ and $R_{j,q}^*$ are the RSEs of q-th measurement for the healthy and inspected structures, respectively. Because the effects of environmental variations are eliminated, the RSE is robust to environmental variations but sensitive to damage compared with the traditional MSE.

3. The statistical hypothesis testing scheme

3.1. Hypothesis testing

The essential paradigm of damage detection is to determine whether the vibration features of the healthy and inspected structures differ significantly. The damage features obtained in each field test are usually not repeatable because of varying environmental and operational conditions. In other words, variation almost always exists between measurements. A damage feature obtained in a field test can thus be considered a random variable; additionally, a set of vibration features obtained from different field tests can be defined as a sample variable, and all possible values of a vibration feature can be defined as a population variable. Therefore, the process of revealing the real state of a structure using statistical methods can be considered a statistical inference approach for damage detection, including estimation and hypothesis testing. In this study, a statistical hypothesis testing scheme is adopted for damage detection. The objective is to decide whether measurements of the inspected structure indicate a departure from the previously established normal condition or, more specifically, to examine whether the distribution of the RSE samples that are obtained from the inspected structure is related to the distribution for the healthy structure.

In the following sections, the RSEs for the healthy and inspected structures, denoted by R_j and R_j^*, respectively, are regarded as two random variables used for hypothesis testing. It is assumed that the random variable R_j has a normal distribution with unknown mean μ_j and unknown standard deviation σ_j, i.e., $R_j \sim \mathcal{N}\left(\mu_j, \sigma_j^2\right)$, similarly for the inspected

structure, $R_j^* \sim \mathcal{N}\left(\mu_j^*, \sigma_j^{*2}\right)$. The analysis aims to test whether these two means are equal, namely, does $\mu_j = \mu_j^*$. Therefore, the statistical hypothesis test used herein is as follows.

$$H_0 : \mu_j^* - \mu_j = 0 \tag{12a}$$

$$H_1 : \mu_j^* - \mu_j \neq 0 \tag{12b}$$

Generally, if the result of the test is that the null hypothesis H_0 is rejected, this would indicate the presence of some damage in the structure; otherwise, the inspected structure is healthy. Because $R_{j,1}, R_{j,2}, \cdots, R_{j,q}, \cdots, R_{j,N_q}$ is a series of independent observation of R_j, $\left(R_{j,1}, R_{j,2}, \ldots, R_{j,q}, \ldots, R_{j,N_q}\right)$ is a sample of R_j. Likewise, $\left(R_{j,1}^*, R_{j,2}^*, \ldots, R_{j,q}^*, \ldots, R_{j,N_q}^*\right)$ is a sample of R_j^*. Student's t-test is traditionally performed to compare two normally distributed samples. If the variances of random variables R_j and R_j^* are similar, namely, $\sigma_j^2 \approx \sigma_j^{*2}$, the risk of the test is determined following a standardized t-distribution with $2N_q - 2$ degrees of freedom. A limitation of Student's t-test is associated with the condition of homoscedasticity among samples. Estimated variances in two samples are not always homogeneous, and Student's t-test cannot be used systematically. Welch [36] proposed a variant of the t-test, and the corresponding test statistic for the comparison of the healthy and inspected structures is defined as

$$T_j = \frac{\overline{R}_j^* - \overline{R}_j}{\sqrt{S_j^2 + S_j^{*2}}/\sqrt{N_q}} \tag{13}$$

where $\overline{R}_j = \frac{1}{N_q}\sum_{q=1}^{N_q} R_{j,q}$ and $S_j = \sqrt[2]{\frac{1}{N_q-1}\sum_{q=1}^{N_q}\left(R_{j,q} - \overline{R}_j\right)^2}$ are the mean and standard deviation of random variable R_j, respectively. Likewise, $\overline{R}_j^* = \frac{1}{N_q}\sum_{q=1}^{N_q} R_{j,q}^*$ and $S_j^* = \sqrt[2]{\frac{1}{N_q-1}\sum_{q=1}^{N_q}\left(R_{j,q}^* - \overline{R}_j^*\right)^2}$ are the mean and standard deviation of R_j^*. For use in hypothesis testing, the distribution of T_j is approximated as a standardized Student's t-distribution.

Welch's t-test takes heteroscedasticity into account by correcting the number of degrees of freedom:

$$\vartheta = \left(N_q - 1\right)\frac{\left(s_j^2 + s_j^{*2}\right)^2}{s_j^4 + s_j^{*4}} \tag{14}$$

where $s_j = \sqrt[2]{\frac{1}{N_q-1}\sum_{q=1}^{N_q}\left(r_{j,q} - \bar{r}_j\right)^2}$ and $s_j^* = \sqrt[2]{\frac{1}{N_q-1}\sum_{q=1}^{N_q}\left(r_{j,q}^* - \bar{r}_j^*\right)^2}$ are the standard deviations of two groups of sample values $r_{j,q}$ and $r_{j,q}^*$ of $R_{j,q}$ and $R_{j,q}^*$, respectively, and $\bar{r}_j = \frac{1}{N_q}\sum_{q=1}^{N_q} r_{j,q}$ and $\bar{r}_j^* = \frac{1}{N_q}\sum_{q=1}^{N_q} r_{j,q}^*$ are the corresponding means.

The value of the test statistic using this method is defined as follows.

$$t_j = \frac{\bar{r}_j^* - \bar{r}_j}{\sqrt{s_j^2 + s_j^{*2}}/\sqrt{N_q}} \tag{15}$$

Thus, the following test can be constructed:

$$\left|t_j\right| \leqslant t_{\varepsilon/2}(\vartheta), \quad \text{Accept } H_0 \tag{16a}$$

$$\left|t_j\right| > t_{\varepsilon/2}(\vartheta), \quad \text{Reject } H_0 \tag{16b}$$

where $t_{\varepsilon/2}$ is such a critical value that the probability is

$$P\left(\left|\frac{\overline{R}_j^* - \overline{R}_j}{\sqrt{S_j^2 + S_j^{*2}}/\sqrt{N_q}}\right| > t_{\varepsilon/2}(\vartheta)\right) = \varepsilon \tag{17}$$

where ε is the chosen risk level for the test.

Table 1
Four scenarios based on hypothesis testing.

Decision	Healthy structure samples	Damaged structure samples
Accept H_0	(a) correct decision	(c) false negative
Reject H_0	(b) false positive	(d) correct decision

3.2. Type I and Type II errors

As listed in Table 1, there are four potential scenarios in hypothesis testing, and the testing samples are categorized as follows: (a) samples from a healthy structure are classified as healthy; (b) samples from a healthy structure are classified as damaged; (c) samples from a damaged structure are classified as healthy; and (d) samples from a damaged structure are classified as damaged.

Here the scenarios (a) and (d) are both correct decisions while scenarios (b) and (c) are two types of misclassification that are described as follows.

- scenario (b): *Type I error* (false positive) is when a structure is healthy but the null hypothesis is rejected and, therefore, the structure is classified as damaged. The probability of committing Type I error is ε, the level of risk.
- scenario (c): *Type II error* (false negative) is when a structure is damaged but the null hypothesis is not rejected and, therefore, the structure is classified as healthy. The probability of committing Type II error is ϵ.

A small risk level ε would lead to a reduced probability of committing Type I error but an increased probability of committing Type II error, and vice versa. A reasonable selection of ε requires a trade-off between the tolerance limits of Type I and Type II errors, as will be discussed in Section 4.5.3.

3.3. The MSR selection strategy

The point worth emphasizing is that all the DoFs of a mode shape are used for the general MSE methods. However, in practice, only three translational DoFs of the structure in the *x*, *y*, and *z* directions (or even only one translational DoF in the *x*- or *y*-direction) can be directly measured by common acceleration and displacement sensors, and the remaining rotational DoFs must be obtained by performing mode shape expansion analysis. A disadvantage of this process is that the rotational DoFs are not necessarily helpful due to their unknown sensitivity to damage; the other is that the mode shape expansion process usually magnifies measurement errors, thereby reducing the accuracy of damage detection. It is, therefore, advisable to only use the translational DoFs to determine the real state of the structure. To more accurately detect damage, an MSR selection strategy is proposed to evaluate the sensitivity of the used MSR matrices to damage, thereby identifying the most sensitive MSR matrix.

Because the state of the inspected structure is determined by Welch's t-test, the accuracy of damage detection depends highly on the sensitivity of T_j to damage. For the n-th structural element, the sensitivity can be obtained by

$$\Omega_{j,n} = \frac{\partial T_j}{\partial \alpha_n} = \frac{\sqrt{N_q}}{\Theta_j^2}\left(\frac{\partial \overline{D}_j}{\partial \alpha_n}\Theta_j - \frac{\partial \Theta_j}{\partial \alpha_n}\overline{D}_j\right) \tag{18}$$

where $\overline{D}_j = \overline{R}_j^* - \overline{R}_j$, $\Theta_j^2 = S_j^2 + S_j^{*2}$, and α_n is the damage severity of the n-th structural element, representing a stiffness reduction ratio of the corresponding undamaged element. Because α_n is not a real-world structural geometric or physical parameter, Eq. (18) seems senseless. To address this issue, it is assumed that damage to a structure can be represented by a decrease in the elasticity modulus of each structural element:

$$E_n^*(\kappa_v) = (1+\alpha_n)\, E_n\,(\kappa_v) \tag{19}$$

where $E_n(\kappa_v)$ and $E_n^*(\kappa_v)$ are the elasticity of the n-th element of the baseline and inspected structures, respectively, at the temperature κ_v. Herein, $E_n(\kappa_v)$ is regarded as a known constant, but $E_n^*(\kappa_v)$ is regarded as an unknown variable. Substituting Eq. (19) into Eq. (18), the derivatives of $\overline{D}_j$ and Θ_j to E_n^* can be obtained as follows:

$$\frac{\partial \overline{D}_j}{\partial \alpha_n} = \frac{E_n(\kappa_v)}{N_q}\sum_{q=1}^{N_q}\frac{\partial D_{j,q}}{\partial E_n^*(\kappa_v)} \tag{20}$$

where $D_{j,q} = R_{j,q}^* - R_{j,q}$ and

$$\frac{\partial \Theta_j}{\partial \alpha_n} = \frac{E_n(\kappa_v)}{(N_q-1)\Theta_j}\sum_{q=1}^{N_q}\left(R_{j,q}^* - \overline{R}_j^*\right)\left(\frac{\partial R_{j,q}^*}{\partial E_n^*(\kappa_v)} - \frac{\partial \overline{R}_j^*}{\partial E_n^*(\kappa_v)}\right) \tag{21}$$

The sensitivity of T_j with respect to α_n can obtained by substituting Eqs. (20) and (21) into Eq. (18).

$$\Omega_{j,n} = \frac{E_n(\kappa_v)}{\sqrt{\Theta_j^2 N_q}}\left\{\sum_{q=1}^{N_q}\frac{\partial D_{j,q}}{\partial E_n^*(\kappa_v)} - \frac{N_q\overline{D}_j}{(N_q-1)\Theta_j^2}\sum_{q=1}^{N_q}\left[\left(R_{j,q}^* - \overline{R}_j^*\right)\left(\frac{\partial R_{j,q}^*}{\partial E_n^*(\kappa_v)} - \frac{\partial \overline{R}_j^*}{\partial E_n^*(\kappa_v)}\right)\right]\right\} \tag{22}$$

The main step in calculating the sensitivity is to compute $\partial R_{j,q}^*/\partial E_n^*(\kappa_v)$. Considering the definition of RSE, namely, $R_{j,q}^* = \left(\psi_{j,q}^*\right)^T \mathbf{K}\psi_{j,q}^*$, one can expand $\partial R_{j,q}^*/\partial E_n^*(\kappa_v)$ as

$$\frac{\partial R_{j,q}^*}{\partial E_n^*(\kappa_v)} = \frac{\partial\left(\psi_{j,q}^*\right)^T}{\partial E_n^*(\kappa_v)}\mathbf{K}\psi_{j,q}^* + \left(\psi_{j,q}^*\right)^T\frac{\partial \mathbf{K}}{\partial E_n^*(\kappa_v)}\psi_{j,q}^* + \left(\psi_{j,q}^*\right)^T\mathbf{K}\frac{\partial \psi_{j,q}^*}{\partial E_n^*(\kappa_v)} \tag{23}$$

but $\left(\psi_{j,q}^*\right)^T\frac{\partial \mathbf{K}}{\partial E_n^*(\kappa_v)}\psi_{j,q}^* = 0$ because the overall stiffness matrix of the baseline structure is dependent on elasticity modulus of the inspected structure. Because $\mathbf{K}$ is a symmetric matrix, one thus obtains

$$\left[\frac{\partial\left(\psi_{j,q}^*\right)^T}{\partial E_n^*(\kappa_v)}\mathbf{K}\psi_{j,q}^*\right]^T = \left(\psi_{j,q}^*\right)^T\mathbf{K}\frac{\partial \psi_{j,q}^*}{\partial E_n^*(\kappa_v)} \tag{24}$$

Also, $\frac{\partial\left(\psi_{j,q}\right)^T}{\partial E_n^*(\kappa_v)}\mathbf{K}\psi_{j,q}^*$ is a scalar with a transpose equal to itself as follows.

$$\left[\frac{\partial\left(\psi_{j,q}^*\right)^T}{\partial E_n^*(\kappa_v)}\mathbf{K}\psi_{j,q}^*\right]^T = \frac{\partial\left(\psi_{j,q}^*\right)^T}{\partial E_n^*(\kappa_v)}\mathbf{K}\psi_{j,q}^* \tag{25}$$

By comparing Eqs. (24) and (25), one can obtain $\frac{\partial\left(\psi_{j,q}^*\right)^T}{\partial E_n^*(\kappa_v)}\mathbf{K}\psi_{j,q}^* = \left(\psi_{j,q}^*\right)^T\mathbf{K}\frac{\partial \psi_{j,q}^*}{\partial E_n^*(\kappa_v)}$, and Eq. (23) reduces to

$$\frac{\partial R_{j,q}^*}{\partial E_n^*(\kappa_v)} = 2\left(\psi_{j,q}^*\right)^T\mathbf{K}\frac{\partial \psi_{j,q}^*}{\partial E_n^*(\kappa_v)} \tag{26}$$

Here, the method provided by Yan and Ren [12] and Yan et al. [13] is used to derive a closed-form sensitivity formula of $R_{j,q}^*$ with respect to $E_n^*(\kappa_v)$. Eq. (26) can be rewritten into a compact matrix form

$$\frac{\partial R_{j,q}^*}{\partial E_n^*(\kappa_v)} = 2\left[\left(\psi_{j,q}^*\right)^T\mathbf{K} \quad \mathbf{0}\right]\begin{Bmatrix}\frac{\partial \psi_{j,q}^*}{\partial E_n^*(\kappa_v)} \\ \frac{\partial \lambda_{j,q}^*}{\partial E_n^*(\kappa_v)}\end{Bmatrix} \tag{27}$$

Lee and Jung [37] presented the eigenpair derivations to obtain the elasticity modulus as follows.

$$\begin{Bmatrix}\frac{\partial \phi_{j,q}^*}{\partial E_n^*(\kappa_v)} \\ \frac{\partial \lambda_{j,q}^*}{\partial E_n^*(\kappa_v)}\end{Bmatrix} = \begin{bmatrix}\mathbf{K}^* - \lambda_{j,q}^*\mathbf{M}^* & -\mathbf{M}^*\phi_{j,q}^* \\ -\left(\phi_{j,q}^*\right)^T\mathbf{M}^* & 0\end{bmatrix}^{-1}\begin{Bmatrix}-\left(\frac{\partial \mathbf{K}^*}{\partial E_n^*(\kappa_v)} - \lambda_{j,q}^*\frac{\partial \mathbf{M}^*}{\partial E_n^*(\kappa_v)}\right)\phi_{j,q}^* \\ \frac{1}{2}\left(\phi_{j,q}^*\right)^T\frac{\partial \mathbf{M}^*}{\partial E_n^*(\kappa_v)}\phi_{j,q}^*\end{Bmatrix} \tag{28}$$

where $\mathbf{M}^*$ and $\mathbf{K}^*$ are the overall mass and stiffness matrices of the inspected structure. Likewise, as for the MSR $\psi_{j,q}^*$, one can obtain

$$\begin{Bmatrix}\frac{\partial \psi_{j,q}^*}{\partial E_n^*(\kappa_v)} \\ \frac{\partial \lambda_{j,q}^*}{\partial E_n^*(\kappa_v)}\end{Bmatrix} = \begin{bmatrix}\mathbf{K}^* - \lambda_{j,q}^*\mathbf{M}^* & -\mathbf{M}^*\psi_{j,q}^* \\ -\left(\psi_{j,q}^*\right)^T\mathbf{M}^* & 0\end{bmatrix}^{-1}\begin{Bmatrix}-\left(\frac{\partial \mathbf{K}^*}{\partial E_n^*(\kappa_v)} - \lambda_{j,q}^*\frac{\partial \mathbf{M}^*}{\partial E_n^*(\kappa_v)}\right)\psi_{j,q}^* \\ \frac{1}{2}\left(\psi_{j,q}^*\right)^T\frac{\partial \mathbf{M}^*}{\partial E_n^*(\kappa_v)}\psi_{j,q}^*\end{Bmatrix} \tag{29}$$

Here, provided that the stiffness and mass distributions of the inspected structure are almost the same as those of the baseline structure, that is, $\mathbf{K}^* \approx \mathbf{K}$ and $\mathbf{M}^* \approx \mathbf{M}$, and noting that $\partial \mathbf{M}^*/\partial E_n^*(\kappa_v) = \mathbf{0}$ and $\partial \mathbf{K}^*/\partial E_n^*(\kappa_v) = \partial \mathbf{K}/\partial E_n(\kappa_v) = \mathbf{K}/E_n(\kappa_v) = \mathbf{K}_n^0$, Eq. (29) reduces to

$$\begin{Bmatrix}\frac{\partial \psi_{j,q}^*}{\partial E_n^*(\kappa_v)} \\ \frac{\partial \lambda_{j,q}^*}{\partial E_n^*(\kappa_v)}\end{Bmatrix} = \begin{bmatrix}\mathbf{K} - \lambda_{j,q}^*\mathbf{M} & -\mathbf{M}\psi_{j,q}^* \\ -\left(\psi_{j,q}^*\right)^T\mathbf{M} & 0\end{bmatrix}^{-1}\begin{Bmatrix}-\mathbf{K}_n^0\psi_{j,q}^* \\ 0\end{Bmatrix} \tag{30}$$

Substituting Eq. (30) into Eq. (27) yields

$$\frac{\partial R_{j,q}^*}{\partial E_n^*(\kappa_v)} = 2\left[\left(\psi_{j,q}^*\right)^T\mathbf{K} \quad \mathbf{0}\right]\begin{bmatrix}\mathbf{K} - \lambda_{j,q}^*\mathbf{M} & -\mathbf{M}\psi_{j,q}^* \\ -\left(\psi_{j,q}^*\right)^T\mathbf{M} & 0\end{bmatrix}^{-1}\begin{Bmatrix}-\mathbf{K}_n^0\psi_{j,q}^* \\ 0\end{Bmatrix} \tag{31}$$

Similarly, for $\partial \overline{R}_{j,q}^*/\partial E_n^*$ one can find that

$$\frac{\partial \overline{R}_{j,q}^*}{\partial E_n^*(\kappa_v)} = \frac{2}{N_q}\sum_{q=1}^{N_q}\left[\left(\psi_{j,q}^*\right)^T\mathbf{K} \quad \mathbf{0}\right]\begin{bmatrix}\mathbf{K} - \lambda_{j,q}^*\mathbf{M} & -\mathbf{M}\psi_{j,q}^* \\ -\left(\psi_{j,q}^*\right)^T\mathbf{M} & 0\end{bmatrix}^{-1}\begin{Bmatrix}-\mathbf{K}_n^0\psi_{j,q}^* \\ 0\end{Bmatrix} \tag{32}$$

In addition, to compute $\partial D_{j,q}/\partial E_n^*(\kappa_v)$, considering the expression $D_{j,q} = R_{j,q}^* - R_{j,q}$ and the fact that the RSE of the baseline structure is dependent on the elasticity modulus of the inspected structure, $\partial R_{j,q}/\partial E_n^*(\kappa_v) = 0$, and thus the following equation can be obtained.

$$\frac{\partial D_{j,q}}{\partial E_n^*(\kappa_v)} = \frac{\partial R_{j,q}^*}{\partial E_n^*(\kappa_v)} = 2\left[\left(\psi_{j,q}^*\right)^T\mathbf{K} \quad \mathbf{0}\right]\begin{bmatrix}\mathbf{K}-\lambda_{j,q}^*\mathbf{M} & -\mathbf{M}\psi_{j,q}^* \\ -\left(\psi_{j,q}^*\right)^T\mathbf{M} & 0\end{bmatrix}^{-1}\begin{Bmatrix}-\mathbf{K}_n^0\psi_{j,q}^* \\ 0\end{Bmatrix} \tag{33}$$

For simplification, the following equations can be established.

$$\mathbf{H}_{j,q} = \left[\left(\psi_{j,q}^*\right)^T\mathbf{K} \quad \mathbf{0}\right] \tag{34a}$$

$$\mathbf{G}_{j,q} = \begin{bmatrix}\mathbf{K}-\lambda_{j,q}^*\mathbf{M} & -\mathbf{M}\psi_{j,q}^* \\ -\left(\psi_{j,q}^*\right)^T\mathbf{M} & 0\end{bmatrix}^{-1} \tag{34b}$$

$$\mathbf{F}_{j,q,n}^0 = \begin{Bmatrix}-\mathbf{K}_n^0\psi_{j,q}^* \\ 0\end{Bmatrix} \tag{34c}$$

Also noting $\mathbf{K} = \mathbf{K}_n^0 E_n$, one can obtain

$$\mathbf{F}_{j,q,n} = \mathbf{F}_{j,q,n}^0 E_n = \begin{Bmatrix}-\mathbf{K}_n\psi_{j,q}^* \\ 0\end{Bmatrix} \tag{34d}$$

Then, the sensitivity formula of T_j with respect to α_n can be obtained by substituting Eqs. (31) to (34) into Eq. (22).

$$\Omega_{j,n} = \frac{2}{\sqrt{\Theta_j^2 N_q}}\sum_{q=1}^{N_q}\left\{\mathbf{H}_{j,q}\mathbf{G}_{j,q}\mathbf{F}_{j,q,n} - \frac{N_q\overline{D}_j\left(R_{j,q}^* - \overline{R}_j^*\right)}{(N_q-1)\Theta_j^2}\left(\mathbf{H}_{j,q}\mathbf{G}_{j,q}\mathbf{F}_{j,q,n} - \frac{1}{N_q}\sum_{q=1}^{N_q}\mathbf{H}_{j,q}\mathbf{G}_{j,q}\mathbf{F}_{j,q,n}\right)\right\} \tag{35}$$

The overall sensitivity of T_j with respect to all the potential damage in the overall system can be obtained by

$$\Omega_j = \sum_{n=1}^{Ne}\Omega_{j,n} \tag{36}$$

An estimate of Ω_j is therefore computed by substituting the observed sample values into Eq. (37) as follows:

$$\widehat{\Omega}_j = \frac{2}{\sqrt{\left(s_j^2 + s_j^{*2}\right)N_q}}\sum_{q=1}^{N_q}\left\{\mathbf{H}_{j,q}\mathbf{G}_{j,q}\mathbf{F}_{j,q} - \frac{N_q\left(\overline{r}_j^* - \overline{r}_j\right)\left(r_{j,q}^* - \overline{r}_j^*\right)}{(N_q-1)\left(s_j^2 + s_j^{*2}\right)}\left(\mathbf{H}_{j,q}\mathbf{G}_{j,q}\mathbf{F}_{j,q} - \frac{1}{N_q}\sum_{q=1}^{N_q}\mathbf{H}_{j,q}\mathbf{G}_{j,q}\mathbf{F}_{j,q}\right)\right\} \tag{37}$$

where $\mathbf{F}_{j,q} = \sum_{n=1}^{N_e}\mathbf{F}_{j,q,n}$.

For a 3-D offshore platform structure, there are six DoFs for each nodal point. The j-th MSR for q-th measurement of the baseline structure can be expressed as follows.

$$\psi_{j,q} = \left[\cdots, x_{j,q}^{(i)} \quad y_{j,q}^{(i)} \quad z_{j,q}^{(i)} \quad rx_{j,q}^{(i)} \quad ry_{j,q}^{(i)} \quad rz_{j,q}^{(i)}, \cdots\right]^T \tag{38}$$

$\psi_{j,q}$ herein is called a full-domain (f-domain) MSR because it encompasses the modal displacement residual for all 6 DoFs of each nodal point. Two nonfull-domain alternates of $\psi_{j,q}$ that only encompass the modal displacement residual for a translational DoF of each nodal point are defined as follows:

$$\psi_{j,q}^x = \left[\cdots, x_{j,q}^{(i)} \quad 0 \quad 0 \quad 0 \quad 0 \quad 0, \cdots\right]^T \tag{39a}$$

$$\psi_{j,q}^y = \left[\cdots, 0 \quad y_{j,q}^{(i)} \quad 0 \quad 0 \quad 0 \quad 0, \cdots\right]^T \tag{39b}$$

where $\psi_{j,q}^x$ and $\psi_{j,q}^y$ are x- and y-domain MSRs with elements that have nonzero x- and y-translational DoFs, respectively. In other words, the $\psi_{j,q}^x$ and $\psi_{j,q}^y$ are both subsets of $\psi_{j,q}$. Accordingly, the MSR matrices in x- and y-domain can be formed as $\mathbf{\Psi}_j^x = \left[\psi_{j,1}^x, \psi_{j,2}^x, \cdots, \psi_{j,q}^x, \cdots, \psi_{j,N_q}^x\right]$ and $\mathbf{\Psi}_j^y = \left[\psi_{j,1}^y, \psi_{j,2}^y, \cdots, \psi_{j,q}^y, \cdots, \psi_{j,N_q}^y\right]$, respectively. The reason for the selection of these two nonfull alternates of $\psi_{j,q}$ is that they are both of the simplest forms of MSRs and only encompass the modal displacement residual in a translational DoF for each nodal point, which can be directly measured for an offshore platform structure with common biaxial or bidirectional sensors. By the same token, for the inspected structure, the x- and y-domain MSRs denoted

by $\psi_{j,q}^{*x}$ and $\psi_{j,q}^{*y}$, respectively, can both be extracted from the f-domain $\psi_{j,q}^{*}$, and the corresponding MSR matrices $\mathbf{\Psi}_j^{*x}$ and $\mathbf{\Psi}_j^{*y}$ can be correspondingly formed.

The sensitivity Eq. (37) is highly relevant to the j-th MSR of the inspected structure. In return, this formula can serve a pretest tool to select the most sensitive MSR matrix, say $\mathbf{\Psi}_j^{*x}$ or $\mathbf{\Psi}_j^{*y}$ $(j = 1, 2, \cdots, N_m)$, where N_m is the number of available modes. This process selects a damage-sensitive subset of DoFs as well as a mode that maximizes $\widehat{\Omega}_j$. Once the DoF and mode subsets are ascertained, the real state of the inspected structure can be determined by conducting hypothesis testing analysis using the selected MSR matrix.

Following the definition of the RSE formed by the f-domain MSR, the RSEs formed in x- and y-domains of the baseline and inspected structures, respectively, can be constructed as follows.

$$R_{j,q}^{x} = \left(\psi_{j,q}^{x}\right)^{T}\mathbf{K}\psi_{j,q}^{x}; \quad R_{j,q}^{y} = \left(\psi_{j,q}^{y}\right)^{T}\mathbf{K}\psi_{j,q}^{y} \tag{40a}$$

$$R_{j,q}^{*x} = \left(\psi_{j,q}^{*x}\right)^{T}\mathbf{K}\psi_{j,q}^{*x}; \quad R_{j,q}^{*y} = \left(\psi_{j,q}^{*y}\right)^{T}\mathbf{K}\psi_{j,q}^{*y} \tag{40b}$$

Similar to the RSE formed in the f-domain, those formed in the x- and y-domains can also be used to detect damage. The statistical hypothesis testing scheme first involves an analysis of the sensitivity of the test statistic to damage. The sensitivity Eq. (37) can thus be obtained and used to choose the most sensitive MSR matrix. Then, hypothesis testing analysis can be conducted using the selected MSR matrix to determine the real state of the structure. A flowchart to outline the implementation procedures of the statistical hypothesis testing scheme incorporating the MSR selection strategy is given in Fig. 1.

4. Numerical study

An offshore platform structure is used as an illustrative example to explain, validate and test the proposed statistical hypothesis testing scheme. The numerical simulations involved in this study are all conducted in the MATLAB environment.

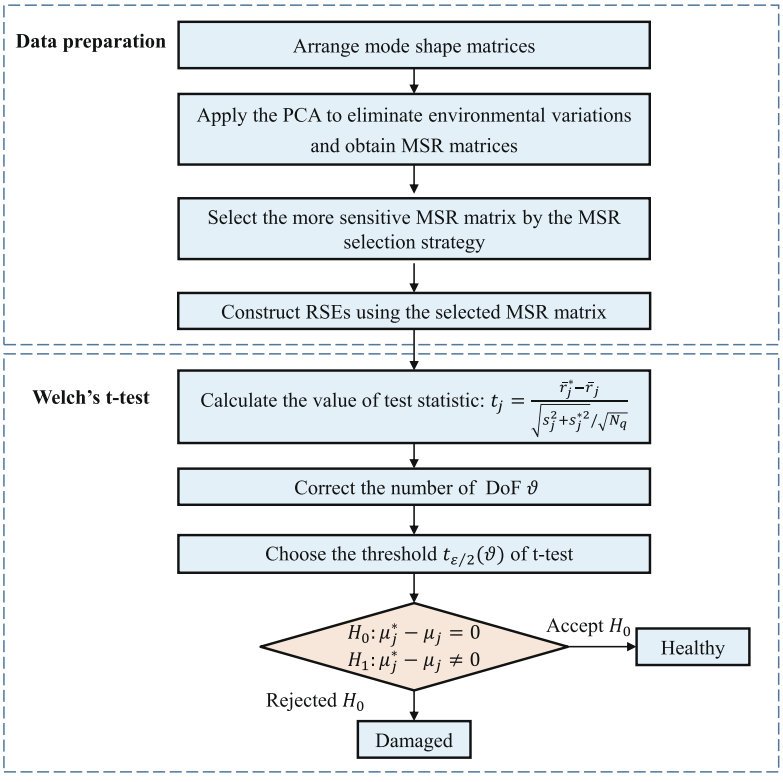

Fig. 1. Flowchart of the statistical hypothesis testing scheme.

4.1. Description of the offshore platform structure

The offshore platform model [34] shown in Fig. 2 is adopted for the numerical study. The model consists of 80 3-D Bernoulli beam elements with a total of 48 nodes, among which the bottom four nodes are fixed. For all structural elements, the mass density $\rho = 7850$ kg/m^3 and Poisson's ratio $\mu = 0.3$. In addition, 300 tons of lumped mass is evenly distributed among nodes Nos. 30, 31, 34, 35 to simulate the top side of the offshore platform. The side lengths of the bottom and top floors of the model are 10.112 m $\times$ 8.764 m and 6.097 m $\times$ 5.284 m, respectively.

The vibration responses of only eight nodes, namely, node Nos. 29 to 35, as shown in Fig. 2, are measured for damage detection, but mode shape expansion analysis to obtain the modal displacements of other nodal points is not performed. In addition, only the effects of temperature variation are considered in the numerical study. A baseline air temperature condition is defined as 20 °C. Under this condition, the healthy offshore platform model is designated as the baseline model. The effect of temperature on the structural modal features is given by Eq. (41). An eigenvalue analysis for the baseline model is carried out, and the obtained first two mode shapes are displayed in Fig. 3, in which the first mode vibrates dominantly in the x-direction and the second mode vibrates in the y-direction. In this study, the first two modes are used for damage detection because very few modes of a real-world offshore platform structure can be excited by natural loads, e.g., waves and ice.

4.2. Damage cases

Five damage cases are investigated in the following numerical simulation, as listed in Table 2. Damage case A is a scenario in which the offshore platform structure is healthy but operates under continuously changing temperature conditions instead of a baseline temperature condition; it can thus be used to test the probability of committing Type I error in the proposed method. Furthermore, to test the probability of committing Type II error, four damage cases are simulated and involve four different types of damaged elements, including element Nos. 8 (a vertical pile element in the vertical plane, VP), 43 (a transverse brace element in the horizontal plane, TB), 67 (a slanted brace element in the vertical plane, VSB), and 71 (a slanted brace element in the horizontal plane, HSB). To investigate the sensitivity of the proposed scheme to damage, it is assumed that these damaged elements all exhibit minor damage with a damage severity of 3%, namely, a 3% stiffness loss.

4.3. The effect of temperature variations

Experimental studies [38] have shown that the elasticity modulus of steel linearly changes with changes in temperature:

$$E_n(\kappa_v) = (1 + \xi)E_n(\kappa_0) \tag{41}$$

where $E_n(\kappa_0)$ is the elasticity modulus of the n-th element at a reference temperature κ_0 and $\xi = \zeta(\kappa_v - \kappa_0)/E_n(\kappa_0)$, in which ζ is a temperature gradient. In this study, the reference temperature κ_0 is selected as the baseline air temperature of 20 °C, the corresponding elasticity modulus $E_n(\kappa_0)$ is 2.06×10^{11} Pa, and the temperature gradient ζ is -1.0×10^8 N/(m^2 · °C).

The structural elements of the offshore platform are exposed to air, water and soil. It is assumed that the air, seawater and soil temperatures synchronously vary, and the relationships between the real air, water and soil temperatures κ_v and local air temperature κ_l are as follow:

$$\kappa_v = a\kappa_l + b \tag{42}$$

where a and b are coefficients of variation; for air, $a = 1$ and $b = 0$; for seawater, $a = 0.45$ and $b = 9$; and for soil, $a = 0.35$ and $b = 1$. The simulated real ambient temperatures versus the local air temperature are plotted in Fig. 4.

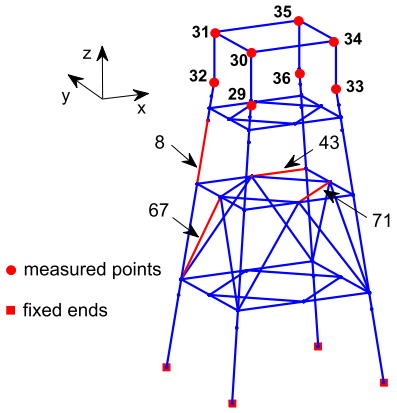

Fig. 2. Sketch of the offshore platform structure.

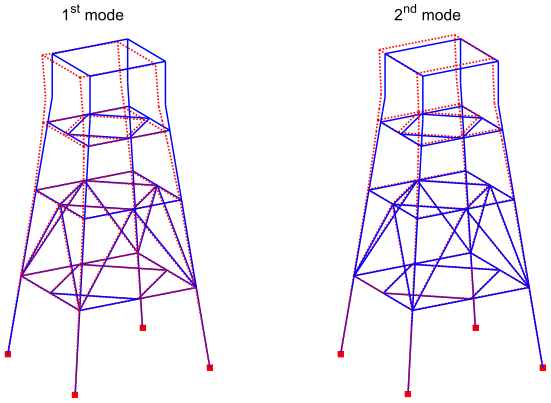

Fig. 3. The first two mode shapes of the baseline offshore platform.

Furthermore, when a structural element is simultaneously affected by damage and temperature changes, the elasticity modulus of the element can be obtained by substituting Eq. (41) into Eq. (19).

$$E_n^*(\kappa_v) = (1+\alpha_n)(1+\xi)E_n(\kappa_0) \tag{43}$$

In this study, the local air temperature is simulated as a normal distribution with a mean value of 20 °C and a standard deviation 1.667 °C, i.e., $\kappa_t \sim \mathcal{N}\left(20, 1.667^2\right)$. Two groups of ambient temperatures for the baseline and inspected structures are simulated. Because a large quantity of measurement data is difficult to obtain in practice for an offshore platform structure based on short-term inspection, only fifty random temperatures are generated for each group. An example of the simulated ambient temperatures for the baseline and inspected structures is shown in Fig. 5. Accordingly, fifty sets of modal shapes corresponding to these fifty random temperatures can be obtained by performing an eigenvalue analysis of both the baseline and inspected structures.

Fig. 6 shows a comparison of the natural frequency changes purely due to damage in the four simulated damage cases and purely due to the temperature changes associated with the 50 simulated random temperatures. Fig. 6 shows that both temperature variations and structural damage are responsible for the changes in the natural frequencies. In some cases, such as damage cases C and E, the effect of temperature variations on the natural frequencies of the structure even masks that of structural damage, highlighting the inhibiting effect of temperature variations in damage detection, especially for HSB and TB elements.

4.4. Numerical results

This section investigates the effectiveness of the proposed statistical hypothesis testing scheme under environmental variations and noise contamination. The effects of noise are simulated by adding Gaussian random error to $\boldsymbol{\Phi}_j$:

$$\tilde{\boldsymbol{\Phi}}_j = \boldsymbol{\Phi}_j + \tau \boldsymbol{\Phi}_j \otimes \boldsymbol{\Xi} \tag{44}$$

where τ is the noise level, and $\tau = 1\%$ in this study unless specified otherwise; $\boldsymbol{\Xi} \in \mathbb{R}^{N_n \times N_q}$ is a noise matrix of random numbers from a standardized normal distribution model; and the operator $\otimes$ represents term-by-term matrix multiplication.

Damage detection analysis for the offshore platform structure is performed first for damage case A, namely, a healthy offshore platform structure operating under continuously changing temperature conditions. The objective of this case is to test the false positive rate of the hypothesis testing scheme. Here, the risk level ε is selected as 0.05, requiring that the state of healthy structure be correctly determined when the resulting $|t_j|$ is less than $t_{0.025}(\vartheta)$.

Table 2
Damage cases in the numerical study.

Damage case	Damage location	Element type	Damage severity	Natural frequencies (Hz)	
				1st	2nd
A	N/A	N/A	N/A	1.0344	1.0423
B	8	VP	3%	1.0336	1.0415
C	43	TB	3%	1.0343	1.0423
D	67	VSB	3%	1.0344	1.0416
E	71	HSB	3%	1.0344	1.0423

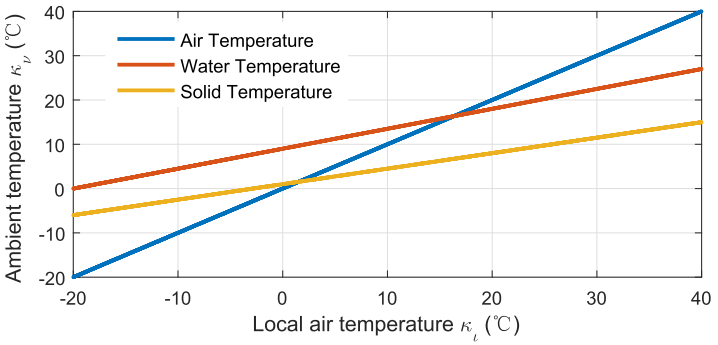

Fig. 4. Ambient temperature variations simulated in this study.

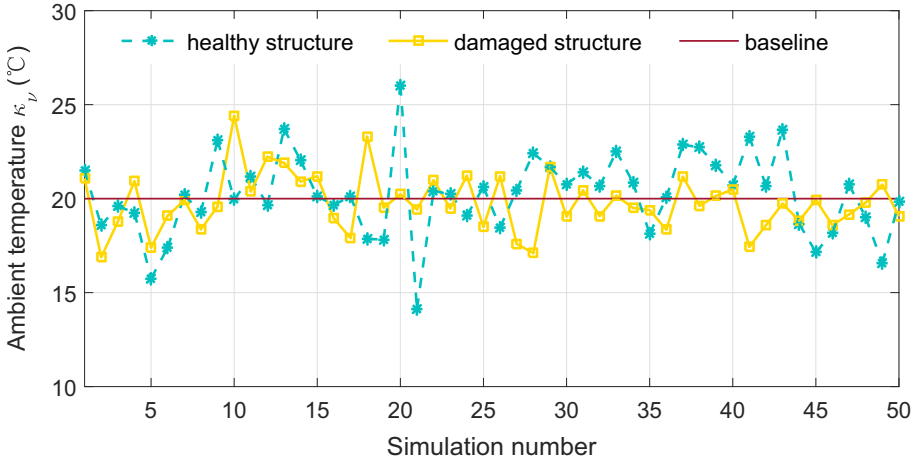

Fig. 5. Simulated ambient temperatures for the baseline and inspected structures.

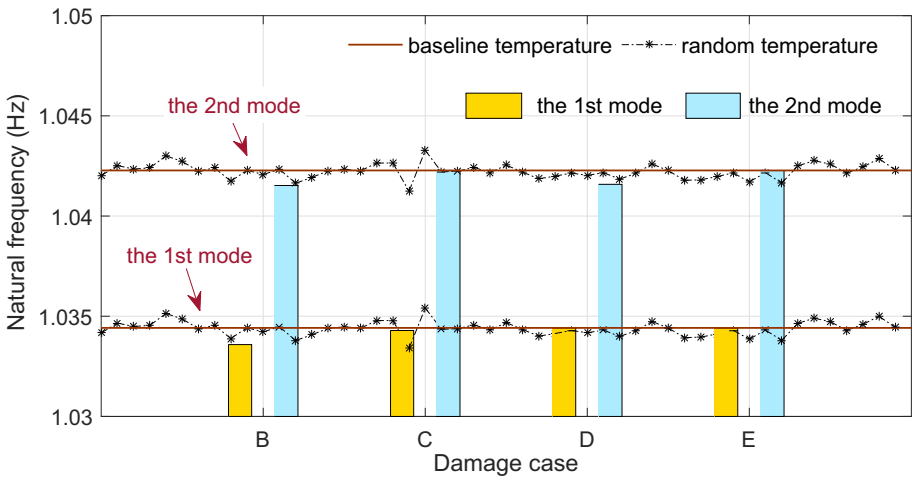

Fig. 6. The first two natural frequencies for damage cases B to E.

An analysis of the sensitivity of the test statistic to damage is conducted to select the proper MSR matrix. Table 3 shows the estimate of sensitivity, i.e., $\widehat{\Omega}_j$, for different MSR matrices. $\boldsymbol{\Psi}_1^{*y}$ and $\boldsymbol{\Psi}_2^{*x}$ have the largest sensitivity to damage when using the first and second modes, respectively.

Table 3
Estimate of damage sensitivity for damage case A.

MSR matrix	$\boldsymbol{\Psi}_1^*$	$\boldsymbol{\Psi}_1^{*x}$	$\boldsymbol{\Psi}_1^{*y}$	$\boldsymbol{\Psi}_2^*$	$\boldsymbol{\Psi}_2^{*x}$	$\boldsymbol{\Psi}_2^{*y}$
$\widehat{\Omega}_j$	4.02e−6	1.83e−5	9.02	2.30e−06	5.68	2.31e−5

Then, the state of the healthy offshore platform structure is determined by statistical hypothesis testing. The first mode is used for damage detection. The probability density function (PDF) of Student's t-distribution versus the test statistic is plotted in Fig. 7, in which the PDFs obtained using different MSR matrices are presented with different colored points. If the resulting t_j falls into the critical region, the null hypothesis that the structure is healthy is rejected in favor of the alternative hypothesis. Fig. 7 shows that all of the estimated test statistics fall outside the critical region, indicating that the statistical hypothesis testing scheme can correctly determine the state of the healthy structure using any of the first MSR matrices.

Then, the second mode is used for damage detection. Fig. 8 shows that the test statistics obtained using $\boldsymbol{\Psi}_2^{*x}$ and $\boldsymbol{\Psi}_2^{*y}$ that fall outside the critical region, indicating excellent agreement between the predicted and real states of the offshore platform structure. However, when using $\boldsymbol{\Psi}_2^*$, Type I error occurs because the test statistic falls inside the critical region, indicating that damage detection using all DoFs does not always result in a satisfactory result.

In addition, upon comparing Figs. 7 and 8 as well as Table 3, no clear correlation between the resulting test statistics and the sensitivity can be observed for the healthy structure. However, the most sensitive MSR matrices, namely, $\boldsymbol{\Psi}_1^{*y}$ and $\boldsymbol{\Psi}_2^{*x}$, can both correctly reveal the state of the healthy structure.

Damage case B is a scenario in which VB element No.8 exhibits a 3% level of damage. Because the real state of the structure is unknown prior to damage detection analysis, the occurrence of Type I error, i.e., the healthy structure is misclassified as damaged, remains to be limited. The risk level ε is still selected as 5% to limit the probability of committing Type I errors no greater than 5%. Thus, for the currently damaged structure, the presence of damage can be identified only if $|t_j|$ is greater than a very large critical value of $t_{0.025}(\vartheta)$. This choice of risk level increases the probability of committing Type II error, i.e., that the currently damaged structure is misclassified as healthy; however, this value is confirmed to be reasonable for the hypothesis testing scheme. The trade-off between Type I and Type II errors will be discussed in Section 4.5.3.

The sensitivity analysis for this damage case suggests that the test statistics associated with $\boldsymbol{\Psi}_1^{*y}$ and $\boldsymbol{\Psi}_2^{*x}$ are most sensitive to damage (see Table 4). It can be inferred that the presence of damage to element No. 8 may be the easiest to identify using $\boldsymbol{\Psi}_1^{*y}$ and $\boldsymbol{\Psi}_2^{*x}$.

Figs. 9 and 10 show the test statistics obtained using the first and second modes, respectively. If the resulting t_j falls into the critical region, the state of the currently damaged structure is correctly revealed. Furthermore, a large $|t_j|$ indicates that the structure has a high probability of damage. These two figures illustrate that the test statistics obtained using $\boldsymbol{\Psi}_1^{*y}$ and $\boldsymbol{\Psi}_2^{*x}$ fall inside the critical region, but other resulting test statistics do not. This observation indicates that the proposed statistical hypothesis testing scheme is effective only when the translational DoFs of each nodal point in a specific direction are used. It is also confirmed that a high damage sensitivity may result in a high probability that the state of the damaged structure is correctly determined; hence, the probability of committing Type II error can be reduced by using the sensitive MSR matrices.

Notably, the t_j value obtained using $\boldsymbol{\Psi}_1^{*y}$ and $\boldsymbol{\Psi}_2^{*x}$ is far greater than zero when the structure is damaged, but for a healthy structure, t_j is approximately zero, confirming that the RSE, as a damage-sensitive feature, significantly increases when the structure is damaged. This property will be used in Section 4.5.3 to select a reasonable critical value $t_{\varepsilon/2}(\vartheta)$.

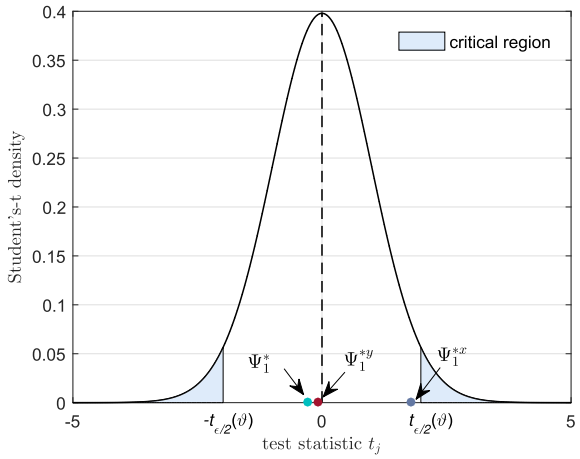

Fig. 7. Results of statistical hypothesis testing using the first mode for damage case A.

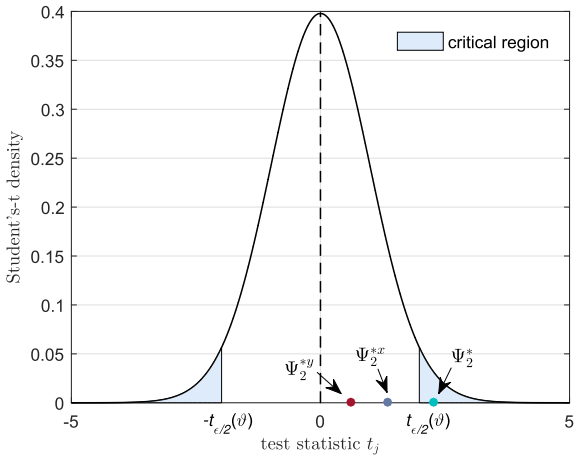

Fig. 8. Results of statistical hypothesis testing using the second mode for damage case A.

Table 5 lists the estimates of sensitivity for damage cases C to E. The table shows that $\boldsymbol{\Psi}_1^{*y}$ and $\boldsymbol{\Psi}_2^{*x}$ are most sensitive to damage, which is surprisingly consistent with the results for damage cases A and B.

Table 6 presents the results of damage detection for damage cases C to E. The table shows that the test statistics obtained using $\boldsymbol{\Psi}_1^{*y}$ and $\boldsymbol{\Psi}_2^{*x}$ are larger than others for the other damage cases, again confirming that high damage sensitivity may result in a large $|t_j|$, thereby reducing the probability of committing Type II error. However, when using the other four MSR matrices, correct decisions may fail to be made in some cases. It is thus reasonable to believe that the MSR selection strategy is effective in choosing sensitive MSR matrices and that the statistical hypothesis testing scheme is capable of identifying the presence of minor damage under environmental variations. It is important to note that the MSR selection strategy enables the use of only the translational DoFs in a low mode for the structure. This approach permits the direct use of the measured vibration responses of sensors without mode shape expansion analysis.

4.5. Parametric study

Furthermore, a parametric study is conducted to investigate the effects of the location and extent of damage, incomplete measurements, and critical value on the performance of the proposed statistical hypothesis testing scheme. The risk level ε is selected as 0.05. $N_t = 1000$ Monte Carlo simulations are performed. The correct detection probability is used to indicate the probability of one making the correct decision:

$$p_d = \frac{N_c}{N_t} \times 100\% \tag{45}$$

where N_c is the number of realizations in which one makes the correct decision regarding the real state of the inspected structure.

4.5.1. Location and extent of damage

To investigate the effects of the location and extent of damage, damage detection analysis is performed by varying the damage level from 0% to 5%. Four damage locations involved in damage cases B to E are analyzed. In most cases, the statistics obtained using $\boldsymbol{\Psi}_1^{*y}$ and $\boldsymbol{\Psi}_2^{*x}$ are most sensitive to damage.

The correct detection probability p_d plotted versus the damage level is presented in Fig. 11. As expected, p_d for each damage location increases as the extent of the damage increases. Overall, when using $\boldsymbol{\Psi}_1^{*y}$ and $\boldsymbol{\Psi}_2^{*x}$, damage can be completely detected at all involved damage locations if the extent of damage is larger than 1%. This finding suggests that the proposed statistical hypothesis testing scheme incorporating the MSR selection strategy is capable of identifying minor damage under temperature variations and noise contamination. Upon comparing the obtained p_d for different damage locations, the presence of damage to VP element No. 8 is easiest to identify, and that for HSB element No. 71 is the most difficult to identify. Notably, the detectability of damage depends highly upon the modal parameter changes that the damage caused. Table 2

Table 4
Estimate of damage sensitivity for damage case B.

MSR matrix	$\boldsymbol{\Psi}_1^{*}$	$\boldsymbol{\Psi}_1^{*x}$	$\boldsymbol{\Psi}_1^{*y}$	$\boldsymbol{\Psi}_2^{*}$	$\boldsymbol{\Psi}_2^{*x}$	$\boldsymbol{\Psi}_2^{*y}$
$\widehat{\Omega}_j$	2.24e−6	1.64e−5	2.10e−3	2.68e−6	1.70e−3	1.62e−5

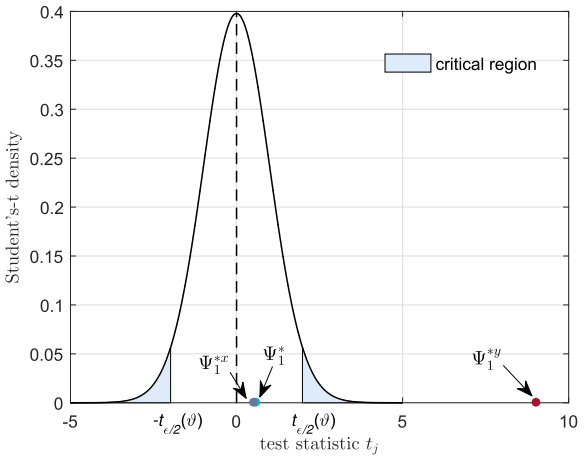

Fig. 9. Results of statistical hypothesis testing using the first mode for damage case B.

shows that the damage to VP element No. 8 causes the largest change in the natural frequencies, thereby resulting in the highest detectability. The same relation is observed for other elements.

It can also be observed that the damage detection performance of the hypothesis testing scheme differs even when using sensitive MSR matrices. Taking TB element No. 43 as an example (see Fig. 11(b)), when the damage level is within the range of [0.0% 1.0%], the p_d value obtained using $\mathbf{\Psi}_1^{*y}$ is larger than that obtained using $\mathbf{\Psi}_2^{*x}$. Specifically, TB element No. 43 is exactly located in the loading path of the first mode of the structure, and when the structure vibrates dominantly in the pattern of the first mode, the element is subjected to combined axial and bending loads; thus, it is an important load-bearing element. The damage to this element, accordingly, causes a large change in the first modal parameter and results in high detectability using $\mathbf{\Psi}_1^{*y}$.

4.5.2. Incomplete measurements

The robustness of the proposed statistical hypothesis testing scheme is highly dependent on the completeness of the measured mode shapes. Although modal expansion is not required, the effect of incomplete measurements on the damage detection results must be investigated, thereby determining the sensor placement for the inspected structure. Four sensor configurations (SCs) are considered and compared in this section.

SC1: Four nodes on the 1st (top) floor of the offshore platform; node Nos. 30, 31, 34, and 35 are instrumented with a uniaxial accelerometer.

SC2: Four nodes on the 2nd floor of the offshore platform; node Nos. 29, 32, 33, and 36 are instrumented with a uniaxial accelerometer.

SC3: Eight nodes on the 1st and 2nd floors of the offshore platform; node Nos. 29 to 36 are instrumented with a uniaxial accelerometer.

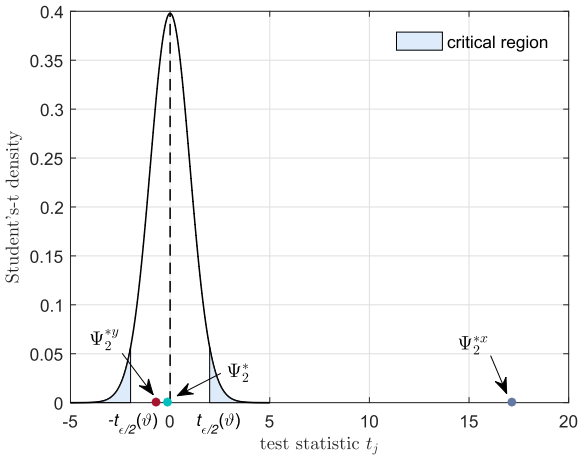

Fig. 10. Results of statistical hypothesis testing using the second mode for damage case B.

Table 5
Estimates of damage sensitivity for damage cases C to E.

Damage case	MSR matrix					
	Ψ_1^*	Ψ_1^{*x}	Ψ_1^{*y}	Ψ_2^*	Ψ_2^{*x}	Ψ_2^{*y}
C	3.75e−6	2.08e−5	5.50e−3	2.19e−6	3.35e−2	2.42e−5
D	2.84e−6	1.92e−5	1.70e−3	2.86e−6	3.36e−2	1.37e−5
E	3.27e−6	1.46e−5	1.32e−1	2.50e−6	2.43e0	1.94e−5

Table 6
Results of damage detection for damage cases C to E.

Damage case	MSR matrix	Ψ_1^*	Ψ_1^{*x}	Ψ_1^{*y}	Ψ_2^*	Ψ_2^{*x}	Ψ_2^{*y}
C	$\lvert t_j \rvert$	2.09	0.29	41.10	0.15	10.37	0.04
	$t_{\varepsilon/2}$	1.98	1.98	1.98	1.99	1.99	1.99
	Decision	√	×	√	×	√	×
D	$\lvert t_j \rvert$	0.09	0.50	16.51	0.36	85.87	1.12
	$t_{\varepsilon/2}$	2.08	2.08	2.08	2.00	2.00	2.00
	Decision	×	×	√	×	√	×
E	$\lvert t_j \rvert$	0.49	0.14	12.41	2.37	11.59	0.93
	$t_{\varepsilon/2}$	1.99	1.99	1.99	2.02	2.02	2.02
	Decision	×	×	√	√	√	×

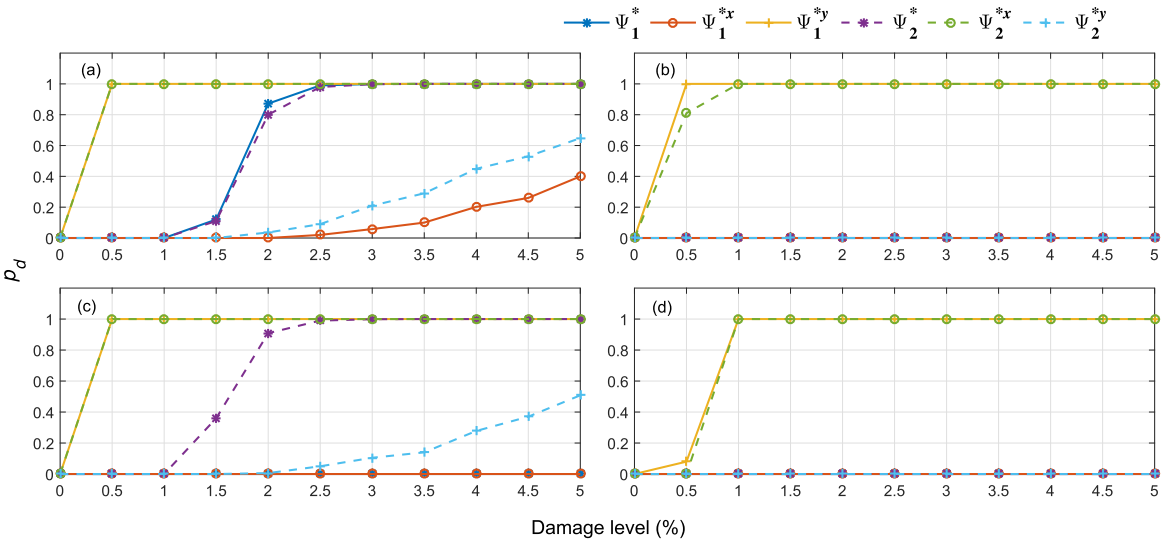

Fig. 11. Correct detection probability plotted versus the damage level based on the damage location: (a) VP element No. 8, (b) TB element No. 43, (c) VSB element No. 67, and (d) HSB element No. 71.

SC4: Every node of the offshore platform is instrumented with a uniaxial accelerometer.

Here, damage case E is used as an example to illustrate the effect of incomplete measurements of the mode shapes on damage detection. Only Ψ_1^{*y} and Ψ_2^{*x} are considered here due to their high sensitivity to damage, and mode shape expansion is not performed. Table 7 shows that regardless of which MSR matrix is used, the p_d value associated with SC1 is better than that associated with SC2 because the nodes on the top floor have the maximum modal displacement and signal-to-noise

Table 7
Correct detection probability for damage case E with different sensor configurations.

MSR matrix	SC1	SC2	SC3	SC4
Ψ_1^{*y}	100%	69%	72%	9%
Ψ_2^{*x}	100%	26%	27%	10%

ratio. Additionally, the result associated with SC3 is slightly better than that associated with SC2. This phenomenon occurs because SC3 can simultaneously collect the data from SC2 and other effective data from SC1. Similarly, the reason that data collected by SC4 fails to result in good damage detection is that SC4 collects considerable ineffective data. Hence, the sensors are expected to be placed on the top floor of the offshore platform structure when using the statistical hypothesis testing scheme.

4.5.3. Critical value

As stressed in Section 3.1, a large critical value $t_{\varepsilon/2}(\vartheta)$ leads to a reduced probability of committing Type I error but an increased probability of committing Type II error, and vice versa. A reasonable selection of $t_{\varepsilon/2}(\vartheta)$ requires a trade-off between the tolerance limits of Type I and Type II errors.

If the values of the test statistic t_j of the undamaged and damaged structures are denoted by t_j^u and t_j^d, respectively, with the aim of simultaneously reducing the probability of committing Type I and Type II errors, the following relation is obtained.

$$\left|t_j^u\right| \leqslant t_{\varepsilon/2}(\vartheta) < \left|t_j^d\right| \tag{46}$$

The numerical results shown in Section 4.4 confirm that the RSE increases when the structure is damaged, and thus, $t_j^d \gg t_j^u \approx 0$. The guideline for selecting $t_{\varepsilon/2}(\vartheta)$ can thus be summarized as finding a range $\mathbb{Q}$ such that

$$t_{\varepsilon/2}(\vartheta) \in \mathbb{Q} = \left[\max\left\{t_j^u\right\}, \min\left\{t_j^d\right\}\right] \tag{47}$$

In this section, because HSB element No. 71 is the most difficult to detect, damage cases A and E are used to investigate the Type I and Type II errors, respectively, that an inappropriate $t_{\varepsilon/2}(\vartheta)$ causes. As before, only $\boldsymbol{\Psi}_1^{*y}$ and $\boldsymbol{\Psi}_2^{*x}$ are employed.

Fig. 12 shows the probability distribution density of t_j (including t_j^u and t_j^d) for damage cases A and E based on 1000 Monte Carlo simulations. As before, the simulated noise and temperature that change the modal features of the structure are both generated from a Gaussian distribution model in each simulation. For the undamaged structure, t_j^u approximately exhibits a normal distribution; specifically, $t_1^u \sim \mathcal{N}\left(0.007, 0.023^2\right)$ and $t_2^u \sim \mathcal{N}\left(0.004, 0.015^2\right)$ using $\boldsymbol{\Psi}_1^{*y}$ and $\boldsymbol{\Psi}_2^{*x}$, respectively. However, for the damaged structure, $t_1^d \sim \mathcal{N}\left(4.519, 0.700^2\right)$ and $t_2^d \sim \mathcal{N}\left(2.571, 20.550^2\right)$. These distributions show that even for a structure in the same damage state, the analysis result varies under different noise and temperature conditions. This phenomenon suggests that the effects of noise and temperature changes on the mode shapes of the structure are not completely eliminated by the PCA algorithm. In other words, the effects of noise and temperature changes are partially reflected in the MSR matrix, which accordingly cannot purely reflect the state of the damaged structure. Additionally, when comparing the distributions of the healthy and damaged structures, the RSE significantly increases when minor damage occurs. The discrepancy range $\mathbb{Q}_{AE} = [0.1, 1.4]$ can be selected as a reasonable $t_{\varepsilon/2}(\vartheta)$ by simultaneously considering the first two modes.

Fig. 12 illustrates that the resulting test statistics for damage cases A and E can be clearly separated in a 1% noise environment. However, in a high noise level environment, these two groups of test statistics cannot be clearly distinguished, resulting in failure to identify the discrepancy range $\mathbb{Q}_{AE}$ by observing the distribution of the test statistics. An effective method to determine the optimal critical value is the use of receiver operating curves (ROCs). These curves represent the trade-off between the false positive rate and the true positive rate for different levels of risk in statistical hypothesis testing. In this analysis, 5% noise is considered, and 100 risk levels within the range [0, 1] are considered with a difference of 0.01. Therefore, 101 connected points are depicted, as shown in Fig. 13. Because the objective of damage detection is minimizing the false positive rate and maximizing the true positive rate, the optimal critical value corresponds to the point on this curve that is nearest to the upper-left corner. Fig. 13 shows that the optimal risk levels are 0.27 and 0.15 for $\boldsymbol{\Psi}_1^{*y}$ and $\boldsymbol{\Psi}_2^{*x}$, respectively, and the corresponding critical values are 1.109 and 1.451.

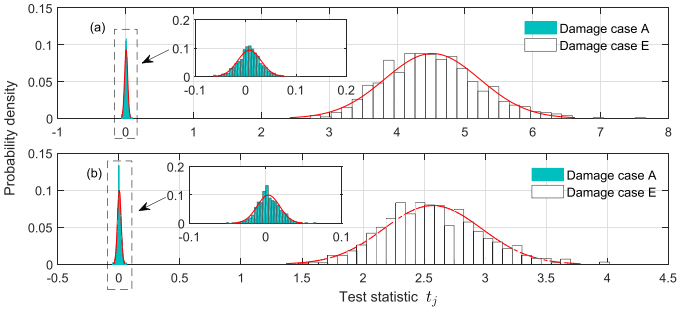

Fig. 12. Distribution of the test statistic for damage cases A and E using (a) $\boldsymbol{\Psi}_1^{*y}$ and (b) $\boldsymbol{\Psi}_2^{*x}$.

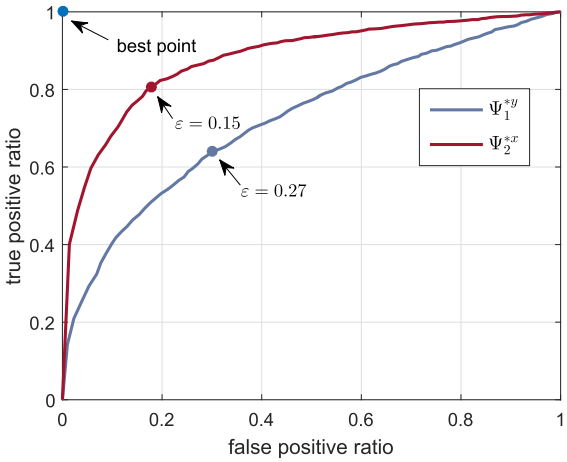

Fig. 13. ROC curves for damage cases A and E using Ψ_1^{*y} and Ψ_2^{*x}.

A key problem to ascertaining the range of $t_{\varepsilon/2}(\vartheta)$ is that the distribution model of t_j^u and t_j^d are unknown or uncertain. In practice, the vibration features of a newly built offshore platform (usually regarded as undamaged) can be measured to obtain two groups of RSE samples that can be used to establish the distribution model of t_j^u. The range of $t_{\varepsilon/2}(\vartheta)$ can be ascertained as $\left[\max\left\{t_j^u\right\}, \max\left\{t_j^u\right\} + \delta\right]$, in which δ is a given threshold representing a trade-off between the Type I and Type II errors. Specifically, a large δ would lead to a reduced probability of committing Type I error but an increased probability of committing Type II error, or vice versa. δ can be determined by the confidence of the users in the safety of the inspected structure. The numerical results shown in Section 4.4 confirm that the RSE is such a damage-sensitive feature that minor damage can result in a large $|t_j|$, so a relatively large δ is recommended with the intention of limiting Type I error.

5. Real-world application

The statistical hypothesis testing scheme was applied for the damage detection of a real-world structure. An offshore wind turbine (see Fig. 14) located in the East China Sea was field tested on August 6 and 7, 2015. This wind turbine was built

Fig. 14. Field-tested wind turbine and sensor configuration.

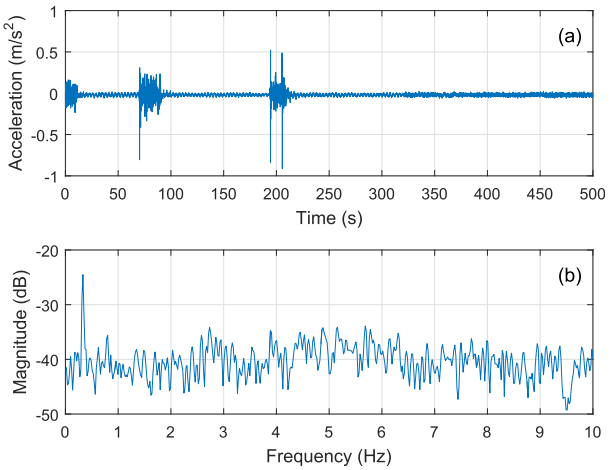

Fig. 15. Example of the acceleration signal collected by S1: (a) signal and (b) magnitude spectrum.

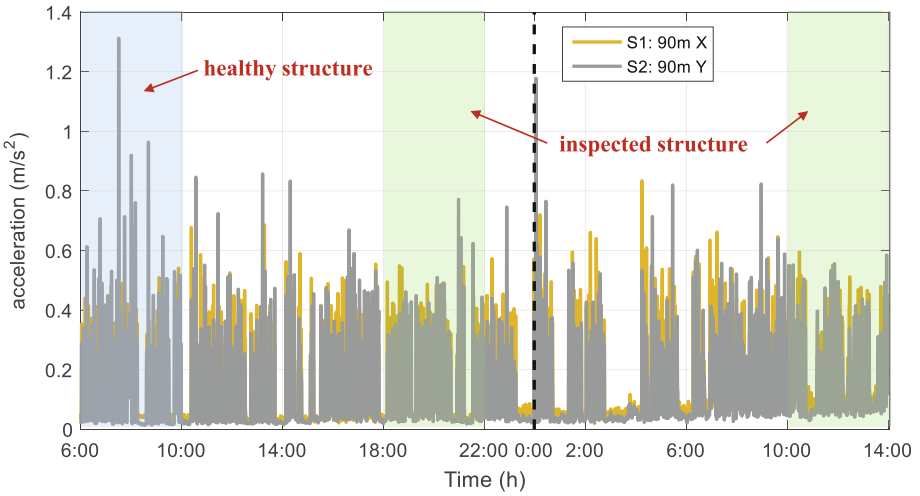

Fig. 16. Acceleration signal collected by S1 for the baseline and test groups.

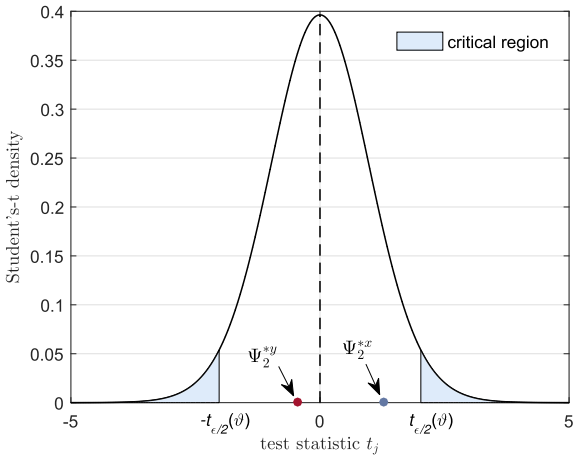

Fig. 17. Results of statistical hypothesis testing using the signal recorded from 6 pm to 10 pm.

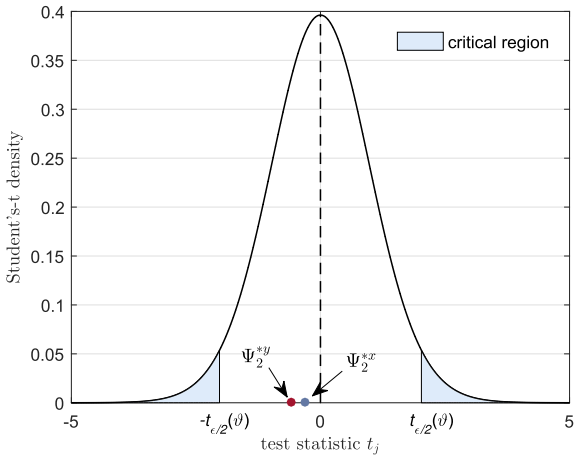

Fig. 18. Results of statistical hypothesis testing using the signal recorded from 10 am to 2 pm.

in February 2015 and operated normally during the test. It has a high-rise pile cap foundation consisting of eight piles. The heights of the wheel hub and the cap are approximately 90 m and 9 m, respectively.

The vibration of the wind turbine was excited by environmental loads, such as wind, wave and current loads, but these loads were not measured. Four biaxial accelerometers (S1, S2, S3 and S4) were installed on the wind turbine tower in the axial direction at heights of 90 m, 63 m, 36 m and 9 m to record the vibration response. The dynamic signal was continuously collected by the data collection instrument G01NET-3 with a frequency sampling rate of 20 Hz. A segment of the signal collected by S1 is shown in Fig. 15. One frequency component, near 0.33 Hz, can be clearly found from the magnitude spectrum of the signal.

In this study, the natural excitation technique (NExT) [39] in conjunction with the eigensystem realization algorithm (ERA) [40] are used to identify the modal parameters (including natural frequencies and mode shapes) of the structure. By performing a NExT-ERA analysis, the second modal parameters of the structure can be identified in each segment of the signals. Therefore, $\boldsymbol{\Psi}_2^{*x}$ and $\boldsymbol{\Psi}_2^{*y}$ are used to construct the RSE samples.

Because the wind turbine was newly built and operated normally, it was regarded as healthy during the tests. However, to validate the effectiveness of the proposed scheme, it was assumed that the structure was healthy at the early stage of the test, but the real state was unknown and needed to be determined in the intermediate and late stages. Accordingly, three groups of measured signals at different measurement times were used in this study. The first group of signals recorded from 6 am to 10 am on August 6 was selected as the reference group, i.e., the data for the healthy structure. The second and third groups of signals recorded in two other time periods were selected as the test groups, i.e., the data for the inspected structure. In each group, 20 sets of modal parameters were identified. The purpose of this study is to ascertain the real state of the inspected structure by examining the deviation between the reference and test groups.

Fig. 16 shows that the second and third groups of signals were selected in two different time periods because the environmental temperature and tide level differed, thereby leading to different effects caused by environmental variations. Although neither the wind speed nor direction was measured, the effect of wind can be reflected by the dynamic response of the structure. The acceleration responses recorded by S1 versus the testing time are plotted in Fig. 16. It can be inferred that there were gusty wind conditions from 6 pm to 10 pm on the first day and continuous wind conditions from 10 am to 2 pm on the second day.

The state of the healthy structure from 6 pm to 10 pm on August 6 was evaluated first. Fig. 17 shows that both of the test statistics obtained using $\boldsymbol{\Psi}_2^{*x}$ and $\boldsymbol{\Psi}_2^{*y}$ fall outside the critical region, indicating that the structure condition is satisfactory. Therefore, the proposed statistical hypothesis testing scheme can correctly reveal the state of the healthy structure under environmental variations even though only the translational DoFs of the measured nodal points were used.

A similar analysis was performed to evaluate the state of the healthy structure from 10 am to 2 pm on August 7. Again, the resulting test statistics indicate that the structure is healthy (see Fig. 18), which agrees with the real state of the structure. Hence, a similar conclusion can be drawn that the proposed statistical hypothesis testing scheme is effective in evaluating

Table 8
Estimates of damage sensitivity in different time periods.

Time period	6 pm to 10 pm		10 am to 2 pm	
MSR matrix	$\boldsymbol{\Psi}_2^{*x}$	$\boldsymbol{\Psi}_2^{*y}$	$\boldsymbol{\Psi}_2^{*x}$	$\boldsymbol{\Psi}_2^{*y}$
$\widehat{\Omega}_j$	6.79e−4	1.40e−5	7.44e−4	1.41e−5

the state of the healthy structure regardless of environmental variations. Additionally, the translational DoFs of the measured nodal points are sufficient for determining the real state of the healthy structure, and the mode shape expansion process is not required.

Then, an analysis of the sensitivity of the test statistic to damage was performed. Table 8 shows that Ψ_2^{*x} is more sensitive to damage than Ψ_2^{*y} in both time periods. However, by comparing Figs. 17 and 18, no clear correlation between the resulting test statistics and the sensitivity can be observed. Therefore, the damage-sensitive MSR matrices are not necessarily preferred for the currently healthy structure.

6. Conclusions

This paper presents a Welch's t-test-based statistical hypothesis testing scheme for structural damage detection under environmental variations. The study identifies the presence of damage by comparing the means of two groups of RSE samples from the healthy and inspected structures. The RSE is constructed based on the MSR, and the effects of environmental variations are eliminated via the PCA method. An MSR selection strategy is proposed to select the damage-sensitive MSR matrix. Additionally, the proposed statistical hypothesis testing scheme only requires the translational DoFs of the MSRs of the structure. This approach permits the direct use of the measured vibration responses of sensors without performing mode shape expansion analysis, which may magnify measurement errors and reduce the accuracy of damage detection.

A numerical offshore platform structure and a real-world wind turbine are used as illustrative examples to explain, validate and test the proposed statistical hypothesis testing scheme. Three main aspects of this approach were emphasized by the results of the numerical study and field test application.

First, the RSE is such a damage-sensitive feature that minor damage can result in a large value of the test statistic. The proposed statistical hypothesis testing scheme is consequently capable of identifying minor damage to different structural elements under environmental variations and noise contamination.

Second, the numerical and field test studies both confirmed that there is no clear correlation between the resulting test statistic and the sensitivity of the test statistic to damage. Therefore, the damage-sensitive MSR matrices are not necessarily required for a healthy structure, although the state of the healthy structure can be correctly revealed by using the sensitive MSR matrices. Moreover, the numerical study confirms that a large damage sensitivity may result in a high probability that the state of the damaged structure is correctly determined; hence, the probability of committing Type II error can be reduced by using the sensitive MSR matrices. Future studies should further validate this conclusion based on real-world applications.

Third, the detectability of damage highly depends upon the selected mode and the modal parameter changes caused by the damage. The mode is appropriate for identifying the presence of damage when the damaged element is located in the loading path of this mode. In addition, for a typical offshore platform structure, the damage to a VP element causes the largest change in the modal parameters of the structure, thereby resulting in the highest detectability. Likewise, damage to an HSB element is the most difficult to detect.

This study assumes that temperature is the main factor that linearly changes the elasticity modulus of structural elements. In reality, environmental conditions affect structural vibration properties in a complicated manner. Many environmental and operational factors are coupled and simultaneously change the dynamic features of structures. Verifying the nonlinear PCA algorithm [23,41] to address multiple environmental factors will be a focus of future work.

Declaration of Competing Interest

The authors declare that they have no known competing financial interests or personal relationships that could have appeared to influence the work reported in this paper.

Acknowledgements

The authors disclose receipt of the following financial supports for the research, authorship, and/or publication of this article: This work is supported by the National Science Fund for Distinguished Young Scholars (51625902), the Major Scientific and Technological Innovation Project of Shandong Province (2019JZZY010820), the National Natural Science Foundation of China (51379196), and the Taishan Scholars Project of Shandong Province (TS201511016).

References

[1] J.E.R. Pérez, R. Rodríguez, A.O. Vázquez-Hernández, Damage detection in offshore jacket platforms with limited modal information using the damage submatrices method, Mar. Struct. 55 (2017) 78–103.
[2] P. Cawley, Closing the gap between research and industrial deployment, Struct. Health Monit. 55 (2018) 78–103.
[3] G. Oliveira, F. Magalhães, C. Álvaro, E. Caetano, Vibration-based damage detection in a wind turbine using 1 year of data, Struct. Control Health Monit. 25 (11) (2018) e2238.
[4] W.J. Yan, M.Y. Zhao, Q. Sun, W.X. Ren, Transmissibility-based system identification for structural health monitoring: fundamentals, approaches, and applications, Mech. Syst. Signal Process. 117 (2019) 453–482.
[5] R. Zhao, R.Q. Yan, Z.H. Chen, K.Z. Mao, P. Wang, R.X. Gao, Deep learning and its applications to machine health monitoring, Mech. Syst. Signal Process. 115 (2019) 213–237.

[6] C. Zhang, L. Cheng, J.H. Qiu, H.L. Ji, J.Y. Ji, Structural damage detections based on a general vibration model identification approach, Mech. Syst. Signal Process. 123 (2019) 316–332.
[7] M.Q. Xu, S.Q. Wang, Y.F. Jiang, Iterative two-stage approach for identifying structural damage by combining the modal strain energy decomposition method with the multiobjective particle swarm optimization algorithm, Struct. Control Health Monit. 26 (2) (2019) e2301.
[8] N. Stubbs, J.T. Kim, Farrar CR. Field, Verification of a nondestructive damage localization and sensitivity estimator algorithm, in: Proceedings of the 13th International Modal Analysis Conference, 1995, pp. 210–218.
[9] S. Park, N. Stubbs, R. Bolton, C. Sikorsky, Field verification of the damage index method in a concrete box-girder bridge via visual inspection, Comput.-Aided Civil Infrastruct. Eng. 16 (1) (2002) 58–70.
[10] Z.Y. Shi, S.S. Law, Structural damage localization from modal strain energy change, J. Sound Vib. 218 (5) (1998) 825–844.
[11] Z.Y. Shi, S.S. Law, L.M. Zhang, Structural damage detection from modal strain energy change, J. Eng. Mech. 126 (12) (2000) 1216–1223.
[12] W.J. Yan, W.X. Ren, A direct algebraic method to calculate the sensitivity of element modal strain energy, Int. J. Numer. Methods Biomed. Eng. 27 (5) (2011) 694–710.
[13] W.J. Yan, W.X. Ren, T.L. Huang, Statistic structural damage detection based on the closed-form of element modal strain energy sensitivity, Mech. Syst. Signal Process. 28 (2012) 183–194.
[14] Y.J. Cha, O. Buyukozturk, Modal strain energy based damage detection using multi-objective optimization, Struct. Health Monit. 5 (2014) 125–133.
[15] Y.J. Cha, O. Buyukozturk, Structural damage detection using modal strain energy and hybrid multiobjective optimization, Comput.-Aided Civil Infrastruct. Eng. 30 (5) (2015) 347–358.
[16] D. Dessi, G. Camerlengo, Damage identification techniques via modal curvature analysis: overview and comparison, Mech. Syst. Signal Process. 52–53 (2015) 181–205.
[17] S.Q. Wang, M.Q. Xu, Modal strain energy-based structural damage identification: a review and comparative study, Struct. Eng. Int. 29 (2) (2019) 234–248.
[18] H. Sohn, K. Worden, C.R. Farrar, Statistical damage classification under changing environmental and operational conditions, J. Intell. Mater. Syst. Struct. 13 (9) (2002) 561–574.
[19] M.G. Wood, Damage analysis of bridge structures using vibrational techniques (Ph.D. thesis), University of Aston, Birmingham, UK, 1992.
[20] B. Peeters, G.D. Roeck, One-year monitoring of the Z24-Bridge: environmental effects versus damage events, Earthq. Eng. Struct. Dyn. 30 (2) (2001) 149–171.
[21] Y. Xia, H. Hao, G. Zanardo, A. Deeks, Long term vibration monitoring of an RC slab: temperature and humidity effect, Eng. Struct. 28 (3) (2006) 441–452.
[22] M. Mahmoud, M. Abe, Y. Fujino, Analysis of suspension bridge by ambient vibration measurement using the time domain method and its application to health monitoring, in: Proc. IMAC XIX, Kissimmee, 2001, pp. 504–510.
[23] T.Y. Hsu, C.H. Loh, Damage detection accommodating nonlinear environmental effects by nonlinear principal component analysis, Struct. Control Health Monit. 17 (3) (2010) 338–354.
[24] B. Peeters, J. Maeck, G.D. Roeck, Vibration-based damage detection in civil engineering: excitation sources and temperature effects, Smart Mater. Struct. 10 (3) (2001) 518–527.
[25] P. Moser, B. Moaveni, Environmental effects on the identified natural frequencies of the Dowling Hall Footbridge, Mech. Syst. Signal Process. 25 (7) (2011) 2336–2357.
[26] Y.Q. Bao, Y. Xia, H. Li, Y.L. Xu, P. Zhang, Data fusion-based structural damage detection under varying temperature conditions, Int. J. Struct. Stab. Dyn. 12 (6) (2012) 1250052.
[27] J. Kullaa, Elimination of environmental influences from damage-sensitive features in a structural health monitoring system, Struct. Health Monit. (2001) 742–749.
[28] E.J. Cross, K. Worden, Q. Chen, Cointegration: a novel approach for the removal of environmental trends in structural health monitoring data, Proc. R. Soc. A: Math. Phys. Eng. Sci. 467 (2133) (2011) 2712–2732.
[29] H. Shi, K. Worden, E.J. Cross, A regime-switching cointegration approach for removing environmental and operational variations in structural health monitoring, Mech. Syst. Signal Process. 103 (2018) 381–397.
[30] A. Deraemaker, E. Reynders, G.D. Roeck, J. Kullaa, Vibration based structural health monitoring using output-only measurements under changing environment, Mech. Syst. Signal Process. 22 (1) (2008) 34–56.
[31] A.M. Yan, G. Kerschen, D.P. Boe, J.C. Golinval, Structural damage diagnosis under varying environmental conditions-part I: a linear analysis, Mech. Syst. Signal Process. 19 (4) (2005) 847–864.
[32] L.E. Mujica, M. Ruiz, F. Pozo, A. Güemes, A structural damage detection indicator based on principal component analysis and statistical hypothesis testing, Smart Mater. Struct. 23 (2) (2013) 025014.
[33] L.E. Mujica, F. Gharibnezhad, J. Rodellar, M. Todd, Considering temperature effect on robust principal component analysis orthogonal distance as a damage detector, Struct. Health Monit. (2019) 1–15.
[34] M.Q. Xu, S.Q. Wang, H.J. Li, A residual strain energy based damage localisation method for offshore platforms under environmental variations, Ships Offshore Struct 14 (7) (2019) 747–754.
[35] J. Morlier, F. Bos, P. Castera, Benchmark of damage localisation algorithms using mode shape data, Key Eng. Mater. 293–294 (2005) 305–312.
[36] B.L. Welch, The significance of the difference between two means when the population variancesare unequal, Biometrika 29 (1938) 350–362.
[37] I.W. Lee, G.H. Jung, An efficient algebraic method for the computation of natural frequency and mode shape sensitivities-Part I. Distinct natural frequencies, Comput. Struct. 62 (3) (1997) 429–435.
[38] C.E. Woon, L.D. Mitchell, Variations in structural dynamic characteristics caused by changes in ambient temperature: I. Experimental, in: Proceedings of SPIE – The International Society for Optical Engineering, 1996, p. 2768.
[39] G.H. James, T.G. Carne, J.P. Lauffer, The natural excitation technique (next) for modal parameter extraction from operating structures, Modal Anal.- Int. J. Anal. Exp. Modal Anal. 10 (4) (1995) 260.
[40] J.N. Juang, R.S. Pappa, An eigensystem realization algorithm for modal parameter identification and model reduction, J. Guidance Control Dyn. 8 (5) (1985) 620–627.
[41] H. Li, S.L. Li, J.P. Ou, H.W. Li, Modal identification of bridges under varying environmental conditions: temperature and wind effects, Struct. Control Health Monit. 17 (5) (2010) 495–512.